

Development and Assessment of a Low Dynamic Vehicle Navigation System

Shahram Moafipoor, Lydia Bock, Jeffrey A. Fayman, Gerry Mader, Paul J. de Jonge
Geodetics, Inc., San Diego, CA

BIOGRAPHIES

Dr. Moafipoor is a navigation scientist, and his focus is on sensor-fusion techniques, new sensor technologies and architectures. His work has included image-based navigation, LiDAR-based navigation, and personal navigation. Dr. Moafipoor has published over 38 peer-reviewed journal articles and conference papers, and numerous technical reports. He is the recipient of five awards, including the 2005 U.S. Geospatial Intelligence Foundation (USGIF) Research Achievement Award. Dr. Moafipoor is a member of the International Association of Geodesy SC4.1 Working Group WG 4.1.2: Indoor navigation systems. Dr. Moafipoor holds a Ph.D. in Geodetic Science from The Ohio State University.

Dr. Lydia Bock is the President and Chief Executive Officer (CEO) of Geodetics Inc. She serves on the board of directors and is one of the original founders of the company. Dr. Bock has 35+ years of industry experience including positions at SAIC and Raytheon. Before co-founding Geodetics, Dr. Bock was an independent business and technology consultant. Dr. Bock's experience spans a wide variety of hi-tech industries including electronics, semiconductors, telecommunications, in the commercial and the defense industries. Dr. Bock holds M.Sc. from Ohio State University and a Ph.D. from Massachusetts Institute of Technology. Dr. Bock won the Raytheon's Micciolli Scholar award, the American Electric Power "operating ideas" award and the Ohio State University Distinguished Alumni Award.

Since 2001, Dr. Jeffrey Fayman has lead Geodetics' Business and Product Development efforts. In this role, Dr. Fayman has driven the technical vision for the company as it expanded from software solution provider, primarily in the civilian market, to a turn-key hardware and software solution provider to the Department of Defense. Dr. Fayman holds a B.A. in business administration, a M.Sc. in Computer Science, and a Ph.D. in Computer Science. Dr. Fayman has published over 35 papers in the fields of precise geo-location, robotics, computer vision and computer graphics.

Dr. Gerald L. Mader currently serves as the Chief of the Geosciences Research Division of the National Geodetic Survey (NGS) and has worked at NGS since 1983. His primary research interests include development of kinematic GPS techniques, ambiguity search algorithms and automated GPS processing. Dr. Mader is President of the International Association of Geodesy's Commission on Space Techniques for Geodesy-GPS Sub commission. Dr. Mader is a co-author of the RINEX format and co-founder of the International GPS Service. He is also the creator of NGS' antenna calibration program and of NGS' On-line Positioning User Service (OPUS).

Dr. Paul de Jonge holds a Ph.D. in Geodetic Engineering from Delft University of Technology. He joined Geodetics in 2000 where his activities include the development and implementation of efficient data processing and quality control techniques for real-time kinematic GNSS applications.

ABSTRACT

There is a need in military operations for reliable, high-accuracy, and low-cost vehicle navigation systems for use in both manned and unmanned ground and air vehicles. Geodetics' Geo-LDV product is an integrated GPS/INS navigation system providing real-time, high-accuracy Time Space Positioning Information (TSPI) in a low-cost, light-weight ruggedized package.

Positioning accuracy in the Geo-LDV is achieved through the use of dual-frequency carrier phase differential GPS solutions provided by Geodetics' Epoch-by-EPOCH® (EBE) technology. EBE performs Precise Instantaneous Network (PIN) positioning utilizing data from one or more GPS reference receivers and the vehicles on-board GPS receiver to produce a rigorous network solution at each measurement epoch. Unlike traditional differential GPS approaches, there is no need for re-initialization immediately following loss-of-lock problems, such as occurs when GPS satellites are occluded from the antennas view. This feature of instantaneous integer ambiguity resolution is of utmost importance when trying to position dynamic platforms operating in environments where GPS reception is lost and regained often, such as in

urban terrain or a maneuvering military aircraft where GPS becomes blocked by airframe masking.

EBE generated GPS solutions are integrated on-board the Geo-LDV with data from a 6-DOF IMU using a loosely-coupled Extended Kalman Filter (EKF). The function of this integration is to propagate the strapdown attitude, inertial velocity and position using the IMU angular rate and acceleration outputs, incorporating EKF corrections. However, since this integration is sensitive to the systematic errors of the IMU, correct modeling of IMU errors is essential for achieving high-accuracy TSPI. In this paper, we focus the approach used in the Geo-LDV for modeling IMU errors. The approach was implemented in an IMU calibration tool box. We present results obtained when the toolbox was used to calibrate several IMU's supported by the Geo-LDV platform.

1. INTRODUCTION

U.S military strategy calls for developing low-cost, robust, and seamless plug-and-play vehicle (ground-based and aircraft) navigation systems. To meet this requirement, Geodetics has recently developed a vehicle navigation system (Geo-LDV) with the goal of obtaining Time Space Positioning Information (TSPI) with better than 20 cm and 0.2° accuracy under low and high dynamics.

Several design options were investigated, but they focused on GPS data (Fayman, *et al.*, 2007). For instance, Geodetics' Attitude Determination System (EADS) employs three GPS receiver/antenna pairs to compute vehicle attitude (heading, pitch, and roll) with an accuracy of 0.05° and position with an accuracy of 5cm (http://www.geodetics.com/publications/9_ITC_VectorFinal08202004.pdf). The main attribute of this design lies in the use of the Epoch-by-Epoch® (EBE) GPS processing technique. EBE performs Precise Instantaneous Network (PIN) positioning utilizing data from one or more GPS reference receivers and the on-board GPS receiver to produce a rigorous network solution at each measurement epoch (Bock, *et al.*, 2004). However, like all GPS-based navigation systems, EADS performance degrades in areas where GPS coverage is diminished or not available, such as urban environments due to GPS satellite and radio data signal blockage, foliage or tunnels.

With the goal of bridging this gap in the new Geo-LDV design, a GPS/Inertial navigation system was developed, which provides real-time, high-accuracy TSPI in a low-cost, light-weight ruggedized package. The current Geo-LDV hardware can accommodate both single and dual frequency GPS measurement engines, a time stamping module to accurately timestamp IMU observations, a microprocessor running the Windows CE operating system, and an external enclosure hosting different IMU

sensors. Three grades of IMU were integrated into the Geo-LDV: a tactical grade Honeywell HG1700, a MEMS-grade Honeywell HG1900, and a low-cost, consumer-grade MicroStrain 3DM-GX2 MEMS IMU.

To integrate the EBE generated GPS solutions with IMU data, a loosely-coupled Extended Kalman Filter (EKF) was developed. The function of this filter is to propagate the strapdown attitude, acceleration, velocity and position using the IMU angular rate and acceleration outputs, incorporating EKF corrections. Since this integration is sensitive to the systematic errors of the IMU, the inertial sensor errors demand careful analysis. Appropriate error modeling of the IMU sensor is also important for maintaining navigation accuracy during GPS outages when the system operates in free inertial mode.

The errors of an inertial sensor are usually categorized into deterministic errors and random errors (Kim, *et al.*, 2004; Naranjo, 2008). A deterministic error will likely produce the same output from a given input-output model from dynamics of the IMU sensor. In contrast, a random error is difficult to predict, and may come from the IMU measurement instrument and/or changes in the operational environment, such as temperature, magnetic fields, dynamic rates, etc. (Jekeli, 2001). IMU calibration is intended to identify and compensate both deterministic and random errors. IMU sensors, like any other mechanical devices, are also subject to aging and degradation from a variety of sources, and require frequent calibration to maintain accuracy.

This paper presents an IMU calibration toolbox designed to calibrate the various IMU sensors used in the Geo-LDV system. The paper also will discuss filter modifications used to incorporate the IMU, an assessment of the error characteristics of IMUs and the overall performance achieved.

We begin with a description of the Geo-LDV hardware with an emphasis on the time-stamping module and accuracy/resolution requirements used to drive the design of the Geo-LDV. Next, we provide an overview on advanced IMU error modeling, highlighting the requirements of in-the-field calibration. The IMU calibration toolbox and numerical results are presented in Section 4. In Section 5, we provide a performance analysis of the Geo-LDV system. Finally, the summary and conclusions are presented in Section 6.

2. Geo-LDV HARDWARE DESIGN

Figure 1 shows a block diagram of the Geo-LDV. Not shown in this figure is the GPS data coming through the data link from terrestrial reference receivers used by the EBE process.

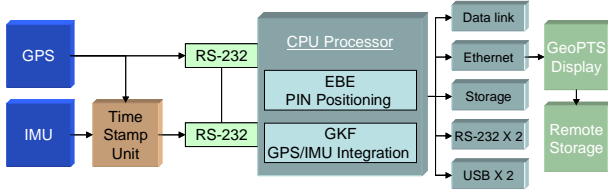


Figure 1: Geo-LDV block diagram

All the components in this configuration, with the exception of the IMU, are packaged into a single self-contained enclosure with a volume of 25 cubic inches. The system is powered by a 24-V nominal external DC supply, with internally regulated DC supply (i.e., 10-36V input). The on-board computer runs the Windows CE operating system, and can support an IMU sample rate of 600 Hz. and a GPS sample rate of 20 Hz. The system is equipped with two RS-232 ports and an Ethernet interface that allows it to be connected to displays, remote storage, and other devices via a TCP/IP network.

To provide accurate IMU time stamps in the Geo-LDV, we have developed a generic approach for accurate time-stamping of any IMU. The Geodetics Time Stamp Unit (Geo-TSU) inserts accurate time-stamps into the IMU standard data streams. The 1 PPS signal from the GPS receiver is used by the Geo-TSU to synchronize the time-stamp value with GPS time. Considering the range of dynamics handled by Geo-LDV, IMU data must be time-stamped with a maximum resolution of 600 Hz. and accuracy of 10 usec. To verify the time stamp accuracy provided by Geo-TSU, we post-processed 14-hours of data collected from an HG1700 IMU (the sensor with the highest sampling rate in our test) and showed that the 100 Hz. time stamping accuracy (mean \pm std) is 0.0100005sec \pm 9.451usec. Figure 2 shows a histogram of the Geo-TSU data in this test.

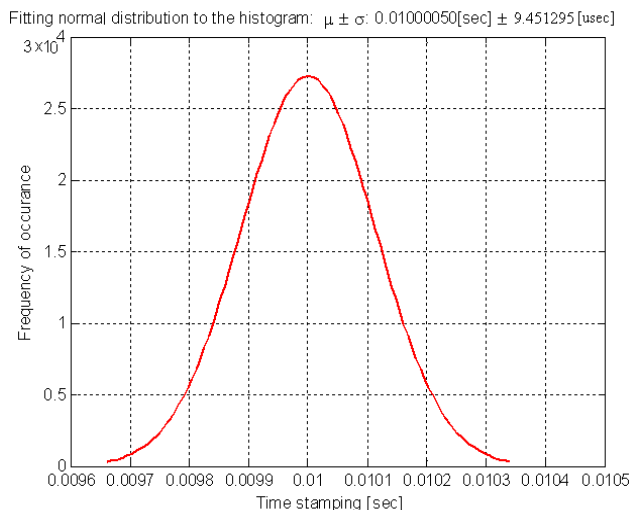


Figure 2: Fitting a normal histogram to Geo-TSU data with 14-hours of collected data

Geo-TSU accuracy can be viewed from two perspectives: 1) the timing offset between the GPS 1 PPS signal and the next IMU signal, and 2) the timing offset between consecutive IMU signals before hitting the next GPS 1 PPS signal. The first offset defines the accuracy of time-stamping, and the second offset defines the precision of time-stamping. Although both offsets are well within the offset expected, the second offset is likely to be more stable than the first as it is caused by the hardware. We performed an error-budget analysis to estimate the delay caused by different components of the hardware. The analysis showed that the most likely sources of delays were the oscillator of the microprocessor and serial to USB interface. This study provided some important insights into the system timing as well as ways to improve the time-stamping accuracy for up to 1 usec. Meanwhile, since 100 Hz. IMU data is 5x the 20 Hz. GPS data rate, the 9.45usec standard deviation was acceptable for use in the Geo-LDV.

3. IMU ADVANCED ERROR-BUDGET ANALYSIS

In this section we present an IMU error-budget analysis for performance validation in real-time operations. Figure 3 summarizes the mathematical relationship between the IMU physical signals and sensory outputs along the sensitivity axes, expressed as a non-linear function of misalignment, sensitivity, bias, and random error terms.

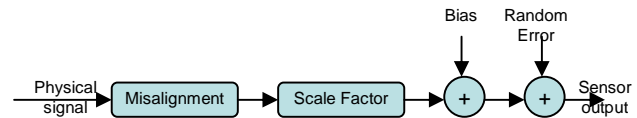


Figure 3: IMU abstract error modeling (Skog and Händel, 2006)

Misalignment results from imperfections in IMU mounting and manufacturing of the IMU's accelerometer/gyros. Misalignment is usually treated as a deterministic error. Scale factor represents the scale of change in the input quantity, and usually results from aging or manufacturing tolerances. The scale factor error is generally divided into two parts: a linear and a nonlinear part. The linear scale factor is treated as deterministic error, and the nonlinear scale factor is treated as random error. The bias term is generally divided into two parts: constant bias and random bias. The constant bias is commonly known as the deterministic error and can be estimated through in-the-field calibration (Hou, 2004).

We begin with an analysis of the deterministic errors (misalignment, linear scale factor, and constant bias), followed by an analysis of the random errors (nonlinear scale factor and random bias).

3.1. DETERMINISTIC ERROR MODELING

Figure 4 illustrates the concept of the misalignment error due to nonorthogonality of IMU axes.

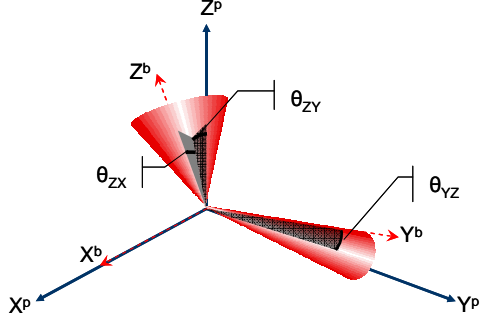


Figure 4: The principle perpendicular frame and tensor frame built by IMU sensitive axes

The IMU accelerometer sensitivity axes measured in the body b-frame, (X^b, Y^b, Z^b) , spans a three dimensional space in the form of a tensor frame. Because of imprecision in the IMU manufacturing process, this tensor frame is not always an orthogonal frame. In order to transform the b-frame to the ideal orthogonal frame, (X^p, Y^p, Z^p) , one can create a relative space (Shin, 2001) for the accelerometers as follows: 1) align X^p with X^b , 2) define the Y^p axis within the $(ZY)^b$ plane to be perpendicular to X^p axis, and 3) express the Z^p axis by successive rotations around X^b and Y^b . Thus, the IMU tensor frame can be aligned with the orthogonal frame by using 3 angles θ_{YZ} , θ_{ZX} , and θ_{ZY} in the symmetric case:

$$\begin{aligned} X^p &= X^b \\ Y^p &= R_Z(\theta_{YZ})Y^b \\ Z^p &= R_x(\theta_{ZX})R_y(\theta_{ZY})Z^b \end{aligned} \quad (1)$$

Since these angles are small, Eq. (1) can be simplified to:

$$\begin{pmatrix} X^p \\ Y^p \\ Z^p \end{pmatrix}_{accel} = \begin{pmatrix} 1 & -\theta_{YZ} & \theta_{ZY} \\ 0 & 1 & -\theta_{ZX} \\ 0 & 0 & 1 \end{pmatrix} \begin{pmatrix} X^b \\ Y^b \\ Z^b \end{pmatrix}_{accel} \quad (2)$$

To create a gyro perpendicular space relative to the primary perpendicular space built by the accelerometer frame, an additional direction cosine matrix is defined to transform the gyro axes into the platform coordinate system (Skog and Händel, 2006). Eq. (3) expresses the misalignment model of gyro axes:

$$\begin{pmatrix} \omega_x^p \\ \omega_y^p \\ \omega_z^p \end{pmatrix}_{gyro} = R_p^b \begin{pmatrix} 1 & -\gamma_{YZ} & \gamma_{ZY} \\ 0 & 1 & -\gamma_{ZX} \\ 0 & 0 & 1 \end{pmatrix} \begin{pmatrix} \omega_x^b \\ \omega_y^b \\ \omega_z^b \end{pmatrix}_{gyro} \quad (3)$$

where, γ_{YZ} , γ_{ZX} , and γ_{ZY} are small angles required to align the gyro axes with respect to the primary orthogonal frame, and R_p^b is the rotation matrix transforming the gyro axes into the platform body coordinate system, the b-frame.

Adding the deterministic parts of the scale factor and bias terms to the misalignment error, Eq. (4) expresses the total deterministic error models for the accelerometer and gyro measurements triads, provided in the b-frame:

$$\begin{aligned} \bar{f}_{accel}^b &= S_{accel} M_{accel}^{-1} \bar{f}_{accel}^p + \bar{b}_{accel} + \bar{e}_{accel} \\ \bar{\omega}_{gyro}^b &= S_{gyro} M_{gyro}^{-1} R_b^p \bar{\omega}_{gyro}^p + \bar{b}_{gyro} + \bar{e}_{gyro} \end{aligned} \quad (4)$$

where, S_{accel} and S_{gyro} denote 3×3 diagonal matrices, with elements representing the linear scale factor along each axis, M_{accel} and M_{gyro} denote the 3×3 misalignment matrices composed of cross coupling error coefficients expressed by Eqs. (2) and (3), R_b^p is the inverse of R_p^b in Eq. (3),

\bar{b}_{accel} and \bar{b}_{gyro} are 3×1 constant bias vectors, and e_{accel} , e_{gyro} are the noise terms, usually assumed white Gaussian. Note that Eq. (4) has 9 and 12 unknowns for deterministic errors of accelerometers and gyros, respectively.

In order to estimate these deterministic errors, one must precisely measure IMU acceleration and angular rates in a controlled environment. Also, since the accelerometer's output is affected by gravity, it is necessary to know the precise orientation of the IMU with respect to the gravitational field in order to measure the constant bias. In practice, this approach requires lab facilities, such as a rate table, on which the IMU is mounted and several step motors measure its orientation precisely (Dorobantu and Gerlach, 2004; Woodman, 2007; Aslan and Saranlı, 2008). To relax this requirement, we followed the approach proposed by Shin (2001), and Skog and Händel (2006). In this approach, we took advantage of the known magnitude of the measured acceleration and angular velocity for an IMU at rest. Regardless of the orientation and nonorthogonality, the magnitude values sensed by the accelerometer and gyro should be equal to the local normal gravity, $|\bar{g}|$, as a function of location, and the

Earth's rotation rate, $|\bar{\omega}_e| = 7.2921159 \times 10^{-5} \text{ rad/sec}$.

Thus, the primary goal of deterministic error modeling is to evaluate the magnitude of Eq. (4). A least squares solution can be derived by minimizing the quadratic form:

$$\begin{aligned} J_{accel} &= \left\| \Xi \left(\bar{f}_{accel}^b, \xi \right) \right\|^2 - \|\bar{g}\|^2 \\ J_{gyro} &= \left\| \Xi \left(\bar{\omega}_{gyro}^b, \xi \right) \right\|^2 - \|\omega_e\|^2 \end{aligned} \quad (5)$$

where Ξ represents the non-linear function of observations, \bar{f}_{accel}^b or $\bar{\omega}_{gyro}^b$, and unknown deterministic errors, ζ . The linearization of Eq. (5) with respect to the initial unknowns, Ξ_0 , results in a Gauss-Helmert model:

$$w = A\xi + Br \quad (6)$$

where, w is the observational increment, $J|_{\Xi_0}$, the design matrix A denotes the Jacobian matrix of full column rank, $\frac{\partial J}{\partial \xi}|_{\Xi_0}$, ξ represents the corrections to the unknown vector of bias, scale factor, and misalignment of IMU accelerometer/gyro, the observation matrix B is the Jacobian matrix $\frac{\partial J}{\partial \bar{f}_{accel}^b}|_{\Xi_0}$ or $\frac{\partial J}{\partial \bar{\omega}_{gyro}^b}|_{\Xi_0}$, and r is the vector of corrections to the observations. Theoretically, by observing the magnitude of accelerometer/gyro outputs at more than 21 different positions and orientations (9 unknown for accelerometer and 12 unknowns for gyro), Eq. (6) can be solved by the least squares adjustment (Syed, *et al.*, 2007):

$$\hat{\xi} = \left(A^T (BP^{-1}B^T)^{-1} A \right)^{-1} A^T (BP^{-1}B^T)^{-1} w \quad (7)$$

with dispersion and residuals of:

$$D\{\hat{\xi}\} = \sigma_0^2 \left(A^T (BP^{-1}B^T)^{-1} A \right)^{-1}, \quad \tilde{e} = P^{-1}B^T (BP^{-1}B^T)^{-1} w, \quad \hat{\sigma}_0^2 = \frac{\tilde{e}^T P \tilde{e}}{df} \quad (8)$$

However, this approach is impractical if the IMU cannot measure accurate $|\bar{g}|$ or $|\bar{\omega}_e|$. The accuracy of the local normal gravity vector estimate depends on the short term stability of the accelerometer biases and the long term stability of the accelerometer scale factors, whereas the accuracy of the Earth's angular velocity estimate depends only on the short term stability of the gyro biases and scale factors. Since MEMS gyro bias stability is usually less than 0.2°/sec, static data cannot be used to measure Earth's angular velocity. Hence, to estimate deterministic errors of MEMS IMUs, one should replace the physical signal with an oriented system (Zhang, *et al.*, 2010). The numerical tests, shown in Section 4.1, confirm this statement.

3.2. RANDOM ERRORS AND ALLAN VARIANCE ANALYSIS

The Allan variance technique is commonly used to analyze and model moving bias errors of the inertial

sensors used in IMU's. The Allan variance is a statistical model, originally developed to characterize the stability of a time series over an interval of time (IEEE standard). After further developments, this was used to analyze the underlying random error processes of IMUs (Woodman, 2007; Yi, 2007). The basic idea is to take a long sequence of data, collected from a stationary sensor, and divide it into clusters based on an averaging time, τ , as shown in Figure 5.

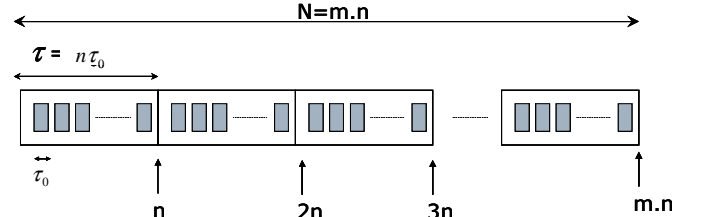


Figure 5: Allan variance and cluster time analysis (Naranjo, 2008)

Assume that there are N consecutive time-series data points, each having a sample time of τ_0 . Associated with each cluster is a time, τ , which is equal to $n\tau_0$. Each cluster is then averaged over the length of that cluster. If the output rate of the IMU sensor is $\Omega(t)$, the cluster average is defined:

$$\bar{\Omega}_{k+\tau}(\tau) = \frac{1}{\tau} \int_{t_k}^{t_k+2\tau} \Omega(t) dt \quad (9)$$

Next, the subsequent cluster averages are calculated over the length of the data:

$$\bar{\Omega}_k(\tau) = \frac{1}{\tau} \int_{t_k}^{t_k+\tau} \Omega(t) dt \quad (10)$$

The Allan variance of length τ is defined as:

$$\sigma^2(t) = \frac{1}{2(N-2n)} \sum_{k=1}^{N-2n} \left(\bar{\Omega}_{k+\tau}(\tau) - \bar{\Omega}_k(\tau) \right)^2 \quad (11)$$

The key to Allan variance analysis is that by assigning different values of time cluster, τ , to Eq. (11), one can obtain a log-log plot, called Allan variance plot. A typical Allan variance plot is shown in Figure 6, where the y-axis is the square root of Allan variance, and x-axis is the time cluster. As seen in this figure, several noise terms can be identified including:

- Quantization noise, Q
- White noise or velocity/angle random walk, N
- Sinusoidal bias, S
- Bias instability or flicker noise, B
- Rate (acceleration/angular) random walk, K
- Drift rate ramp, R

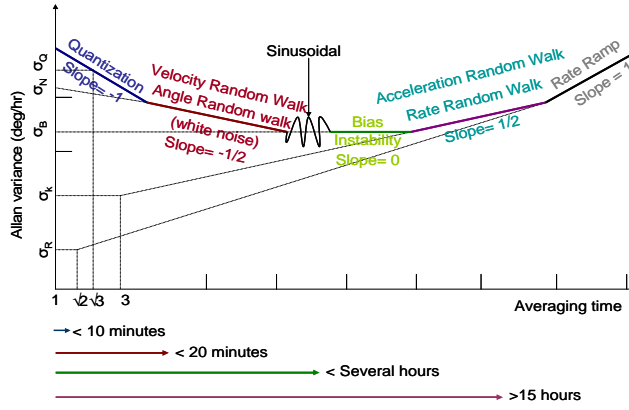


Figure 6: Typical Allan variance analysis plot

These are the principle errors addressed in this paper. In general, any number of random noise components may be present in the data, depending on the type of IMU and the environment in which the data are acquired. Also, some noises may not be recognized by inspection on the Allan variance plot because of overlapping curve patterns and slopes (Zhang, et al., 2008).

Quantization noise is the error resulting from sampling continuous analog signals with finite resolution analog to digital converters. For many MEMS IMUs, quantization noise is the dominant error, and can be measured over a short cluster time. The velocity (angle) random walk, also called white noise, is correlated with thermo-mechanical noise, impacting sensor measurements with high frequency noise and low correlation time. This noise fluctuates at a much higher rate than the sampling rate of the sensor, and appears as a white noise in the velocity (angle) measurements. Sinusoidal noise is resulted from periodic environmental changes and characterized by a number of sinusoidal frequency patterns. Bias instability, or flicker noise is considered low-frequency noise, describing stability of sensor bias over a specified finite sample time. This error can be estimated over a long cluster time. The rate (acceleration/angular) random walk represents exponentially correlated noise with a long correlation time. A longer correlated noise, drift rate ramp, has a quadratic correlation with time cluster, and is often treated as a deterministic error.

From the Allan variance analysis plot, it is clear that the quantization noise and random walk noise are the predominant noise terms in short cluster times, while the rate random walk noise and rate ramp terms exist in long cluster times. Correlation times required for computing each noise term are shown on the bottom of the plot. Table 1 summarizes the information required to estimate each random noise term across different IMU sensors, including noise type, the associated root Allan variance noise, corresponding units, and their slopes in the log-log plot. A more detailed description can be found in, e.g., (Mathur, 1999; Shin, 2001; Naranjo, 2008).

Table 1: Allan variance analysis and random error characteristics

Noise type	Parameter	Gyro unit	Accelerometer unit	Root AV	Curve slope
Quantization	Q	Arcsec	m/hr	$\sigma(\tau) = Q \frac{\sqrt{3}}{\tau}$	-1
Angle (velocity) random walk	N	Deg/vhr	m/s/vhr	$\sigma(\tau) = \frac{N}{\sqrt{\tau}}$	-1/2
Bias instability	B	Deg/hr	m/s/hr	$\sigma(\tau) = B/0.6664$	0
Sinusoidal	ω_b	Deg/hr	m/s/hr	$\sigma(\tau) = \omega_b \left(\frac{\sin^2(\pi f_0 \tau)}{\pi f_0 \tau} \right)$	Sine curve
Angular rate (acceleration) random walk	K	Deg/hr/vhr	m/s/hr/vhr	$\sigma(\tau) = K \sqrt{\frac{\tau}{3}}$	+1/2
Drift rate ramp	R	Deg/hr/hr	m/s/hr/hr	$\sigma(\tau) = R \frac{\tau}{\sqrt{2}}$	+1

The magnitude of each random error, listed in Table 1, can be obtained by intersecting the slope line with the corresponding time cluster, τ . For example, as shown in Figure 6, the drift rate ramp is derived from the slope line at +1 with time cluster at $\sqrt{2}$ hr of averaging time. This allows easy identification of various random noises existing in the data.

3.2.1. IMU ERROR MODELING

Combining the deterministic and random errors discussed in the past two sections, the error models for the accelerometer and gyro are:

$$\begin{aligned}
 \vec{f}_{accel}^b &= \vec{f}_{actual} + \vec{b}_{accel}^{hard} + \vec{b}_{accel}^{moving} + (SF_{accel} + \delta SF_{accel}) \vec{f}_{actual} \\
 &+ M_{accel} \vec{f}_{actual} + \delta \vec{g} + \vec{w}_{accel} \\
 \vec{\omega}_{gyro}^b &= \vec{\omega}_{actual} + \vec{b}_{gyro}^{hard} + \vec{b}_{gyro}^{moving} + (SF_{gyro} + \delta SF_{gyro}) \vec{\omega}_{actual} \\
 &+ M_{gyro} \vec{\omega}_{actual} + \vec{w}_{gyro}
 \end{aligned} \tag{12}$$

The bias term, \vec{b} , is split into two parts: a constant, or hard bias, \vec{b}^{hard} , which is treated as a deterministic error, and a random, or bias drift, \vec{b}^{moving} , which is treated as a random error. The linear scale factor, SF , is initialized in deterministic error processing, and its residual, δSF , is treated as a random error. Misalignment is generally treated as a deterministic error in the error equation model. The noise error, w , is the wide band sensor noise, assumed to be normally distributed. The gravity error, $\delta \vec{g}$, expresses gravity anomalies and deflection of the vertical (DOV). This disturbance state is usually modeled as a first-order Gauss-Markov process. The moving bias term represents the overall magnitude of random biases listed in Table 1.

Assigning one moving bias term in error modeling is only reasonable for high grade IMUs. For other IMUs, the moving bias term requires an accurate error-budget analysis.

4. IMU CALIBRATION TOOLBOX AND NUMERICAL RESULTS

We have developed an IMU calibration toolbox to estimate the errors described in Section 3. We gathered data from various IMU's and used our toolbox to estimate their errors. In this section, we show the results of our analysis. First, the deterministic errors are estimated using a modified least squares model. Next, the stochastic components of the moving bias term listed in Table 1 are evaluated using the Allan variance analysis.

4.1. DETERMINISTIC ERRORS

For our short-term error study, one hour of static data was collected at room temperature, 65°F, from a Honeywell HG1700 IMU. The IMU was placed into more than 13 different orientations. At each orientation, more than 500 samples at the IMU rate of 100 Hz. were acquired.

As shown in Eqs. (5) and (6), the linearized equation results in a Gauss-Helmert model, with unknowns of constant bias, scale factor, and misalignment of IMU accelerometers and gyros. However, after establishing the Gauss-Helmert model and associated matrices, it was found that the model was rank-deficient, indicating a lack in the system observability. The study showed that the singular values were related to the eigenvalues of the misalignment terms. This deficiency also was observed by Skog and Händel (2006), confirming the fact that the misalignment estimation requires an oriented system; otherwise, the physical signal noise dominates the evolving observation components.

An alternative approach for obtaining a stable solution is to retain the smaller, problematic eigenvalues, but weight them by the addition of a small, positive constant to dampen their effects on the linear system. This method is referred to as Total Least Squares (TLS). The TLS is an extension of the usual least squares estimation, which handles uncertainties in both observation and design matrices (Schaffrin, 2006). The uncertainty is introduced as an error variance (EV) and added to Eq. (7) as:

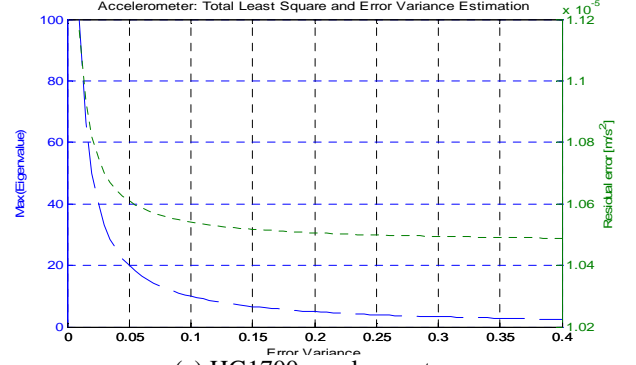
$$\hat{\xi} = \left(A^T (BP^{-1}B^T)^{-1} A + EV * I \right)^{-1} A^T (BP^{-1}B^T)^{-1} w \quad (13)$$

with an uncertainty:

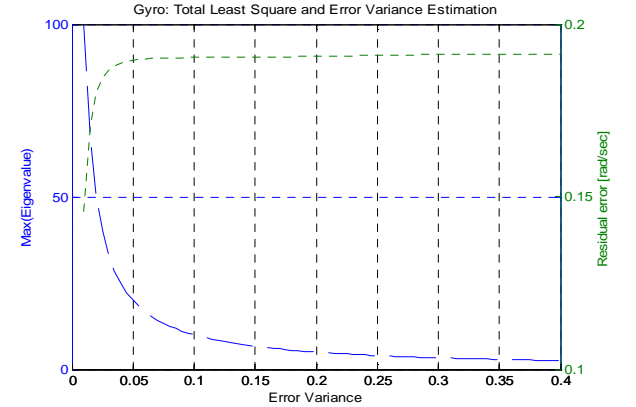
$$D\{\hat{\xi}\} = \sigma_0^2 \left(A^T (BP^{-1}B^T)^{-1} A + EV * I \right)^{-1} * \left(A^T (BP^{-1}B^T)^{-1} A \right) * \left(A^T (BP^{-1}B^T)^{-1} A + EV * I \right)^{-1} \quad (14)$$

In an ill-conditioned model, an appropriate choice of the damping factor EV will reduce solution variance, and hence substantially improve the mean-squared error of estimation. Thus, the problem reduces to finding a value

for the EV, which is just large enough to stabilize the solution, but small enough to minimize the predictive properties of the solution. To this end, a range of EV's from 0 to 0.4 were simulated and introduced to Eq. (13). Figure 7 shows the trade off in EV and maximum eigenvalues of the normal matrix as well as the residual error, \bar{e} .



(a) HG1700 accelerometer



(b) HG1700 gyro

Figure 7: TLS and error variance simulation

The EV value of 0.05 was chosen, because beyond this value, as seen in Figure 7, the accelerometer/gyro solutions become steady state. For the accelerometer, this value also meets the minimum error. To minimize the gyro error, one also needs to observe the eigenvalues. Indeed, the effectiveness of the EV depends greatly on the eigenvalues. Table 2 summarizes the deterministic errors estimated for the HG1700 IMU used in the test.

Table 2: HG1700 IMU and deterministic error estimation

HG1700 IMU		X-axis	Y-axis	Z-axis
Accel	Hard bias [m/s ²]	9.609288 e-05	-1.621417 e-05	-1.405595 e-04
	Scale factor	1.0000005	0.9999886	1.0013825
Gyro	Hard bias [rad/s]	0.0071331	0.0008607	0.0120975
	Scale factor	0.9975054	0.9999996	0.9999273

To avoid these complexities, some researchers have equated the hard bias with the mean of the sensor outputs, and the scale factor with unit vector (Flenniken, 2005).

4.2. RANDOM ERRORS

A detailed comparison of the specifications for the IMUs mentioned above, including manufacturer’s stochastic parameters, is provided in Table 3. For a detailed description of the noise specifications and terminology used in Table 3, see Grewal and Andrews (2010). The objective is to compare the estimated error parameters with the manufacturers calibration parameters. When all errors are identified and quantified, the resulting error model will be applied to our loosely coupled GPS/IMU system to bridge the gap between the estimated and published parameters.

For our long-term error study, 16 hours of static data at 100 Hz. were collected at room temperature, 65°F, for both the HG1700 and HG1900 IMUs. Additionally, 5 hours of static data at 20 Hz. at a temperature of 75°F were collected from the MicroStrain MEMS IMU. The IMU measurements are m/s/hr for the accelerometers and deg/hr for the gyros.

Table 3: Manufacturers datasheet; provided by Honeywell Product Brochures: www.honeywell.com and MicroStrain, Technical Product Overview 3DM-GX2, <http://www.microstrain.com/3dm-gx2.aspx>

IMU	HG1700 (AG58)	HG1900 (CA29)	MicroStrain (3DM-GX2)
Gyro Performance			
Bias in-run stability	1°/hr	1°/hr	0.2°/sec for 300°/sec
Bias repeatability (drift)	1°/hr	5°/hr	0.2°/sec
Angular random walk	0.125°/√hr	0.09°/√hr	3.5°/√hr
Quantization	13.47urad	10urad	
Scale factor linearity	150ppm	150ppm	0.2%
Axis alignment stability	500urad	200urad	
Non-orthogonally	100urad	200urad	
Accelerometer Performance			
Bias in-run stability	1.0mg	0.7mg	0.01g for ± 10g range
Bias repeatability	1.0mg	1mg	
Scale factor repeatability	300ppm	300ppm	0.2%
Scale factor linearity	500ppm	500ppm	
Non-orthogonally	100urad	100urad	

4.2.1. HG1700 IMU

For the HG1700, the Allan variance method discussed in Section 3.2, results in the log-log plot of the three axes accelerometer of the root Allan variance shown in Figure 8. It is clear that the quantization noise, Q, is the dominant noise term in short cluster times, while the velocity random walk noise term, N, bias instability, B, and acceleration random walk, K, are the dominant noise terms in long cluster times.

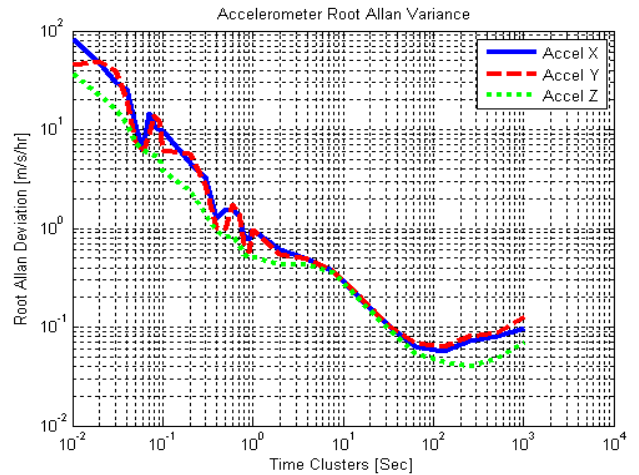


Figure 8: HG1700 accelerometer and Allan variance analysis

This plot also confirms that the z-axis accelerometer has a velocity random walk almost twice that of the other two accelerometers. To read out the existing noise parameters, a straight line with a principle slope, illustrated in Table 1, should be fit to the long cluster time part of the plot. This was achieved with a piecewise line fitting technique. Figure 9 shows the result applied to the accelerometer z-axis. Four lines were formed to recognize random biases, Q, N, B, and K. Note that with real data, gradual transitions exist between the different Allan variance slopes, because of uncertainties that exist in the measurements.

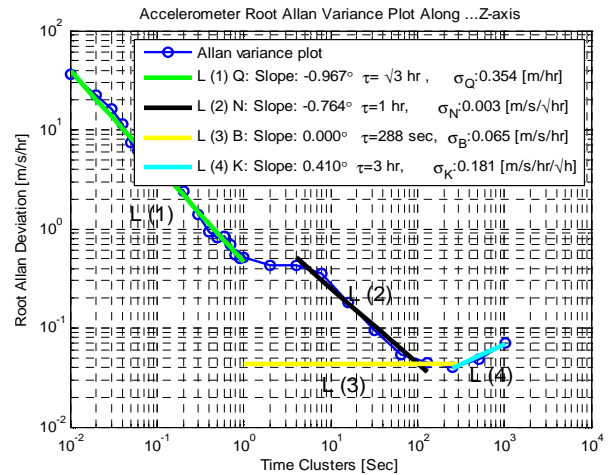


Figure 9: Piecewise line fitting and Allan variance error component analysis

Hence, the HG1700 accelerometer can be modeled as $Q+N+B(\tau)+K$, where Q, N, and K are modeled as Gaussian random walks with independent Gaussian noise variance of σ_Q , σ_N , and σ_K , while the bias instability is modeled as first-order Gauss-Markov process with the corresponding time constant.

Accelerometer quantization variance is generally used to represent the uncertainty in velocity state random walk modeling. The time constant for bias instability was about 288 sec for the accelerometer z-axis, as shown in Figure 9. In other words, after an approximately five minute static period, this bias creates a second-order random walk in vertical velocity with uncertainty that grows proportionally to $t^{3/2}$, and a third-order random walk in altitude that grows proportionally to $t^{5/2}$ (Woodman, 2007). To this end, the bias instability term is usually used to represent the best achievable bias in the fully modeled inertial system. The zero slope line (yellow) fit to the bottom of the curve, determines the upper limit of bias instability. Table 4 shows the estimated noise square-root variance for the accelerometer axes.

Table 4: Allan variance and identified noise square-root variance for the HG1700 accelerometer axes

Accelerometer	X	Y	Z	Average	
Q [m/hr]	0.878	0.540	0.354	0.591	
N [m/s/√hr]	0.004	0.003	0.003	0.003	
B	variance[m/s/hr]	0.090	0.099	0.065	0.085
	time constant [s]	96	96	288	160
K [m/s/hr/√hr]	0.162	0.458	0.181	0.201	

The different errors of the gyros can be characterized through analyzing the log-log plot of the three axes gyro of the root Allan variance, see Figure 10. From the Allan variance plot, it is clear that the quantization noise is the dominant noise for short cluster times, while the angle random walk, represented as wide-band noise, is the primary error source for long cluster times. Thus, the HG1700's gyros can be modeled as Q+N, where Q and N are Gaussian random walks with independent Gaussian noise variance of σ_Q and σ_N . Table 5 lists the estimated noise square-root variance for the gyro axes. The gyro quantization of average 10 arcsec is equal to 48 urad, while this number is specified as 13.47 urad in the manufacturers datasheet, see Table 3.

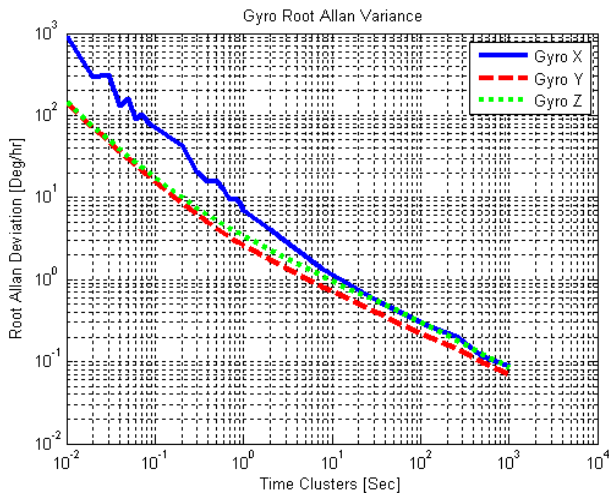


Figure 10: HG1700 gyro and Allan variance analysis

Table 5: Allan variance and identified noise square-root variance for the HG1700 gyro axes

Gyro	X	Y	Z	Average
Q [arcsec]	6.360	7.853	16.687	10.300
N [°/√hr]	0.041	0.037	0.045	0.041

In analogy to the accelerometer quantization variance, the gyro quantization variance is used here to represent the uncertainty of attitude state random walk modeling.

4.2.2. HG1900 IMU

Figure 11 shows the Allan variance plot for accelerometers, and Table 6 summarizes the random errors extracted from the plot. As shown in Table 6, the HG1900 accelerometer is dominated by a short-term quantization noise up to a few seconds, followed by a bias instability up to 26 sec. Next, the measurements degrade due to noise coming from rate random walk. The velocity random walk is usually used to evaluate the sensor noise intensity. The absence of velocity random walk noise (it was insignificant, 0.003 m/s/√hr) and the presence of a long-term rate ramp noise indicates that there is a deterministic bias source in the accelerometer measurements.

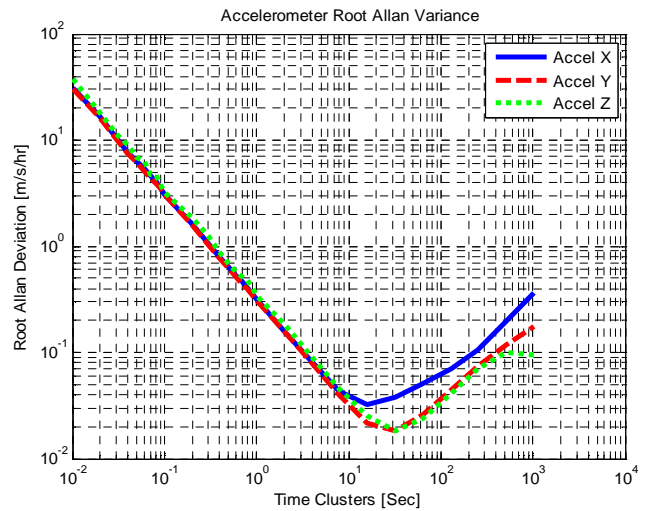


Figure 11: HG1900 accelerometer and Allan variance analysis

Table 6: Allan variance and identified noise square-root variance for HG1900 accelerometer axes

Accelerometer	X	Y	Z	Average	
Q [m/hr]	0.359	0.315	0.376	0.35	
B	variance[m/s/hr]	0.049	0.027	0.028	0.035
	time constant [s]	17	28	33	26
K [m/s/hr/√hr]	0.618	0.951	0.817	0.795	
R [m/s/hr ²]	1.546	-	0.03	0.788	

Thus, it is necessary to identify this constant bias for HG1900 accelerometers and compensate for it in the deterministic error modeling. The nature of the Allan variance plot suggests the HG1900 accelerometer is modeled as $Q+B(\tau)+K+R$.

Similarly, the different errors of the HG1900 gyros can be characterized by analyzing the Allan variance plot in Figure 12. Table 7 lists all the identifiable error coefficients for the gyros.

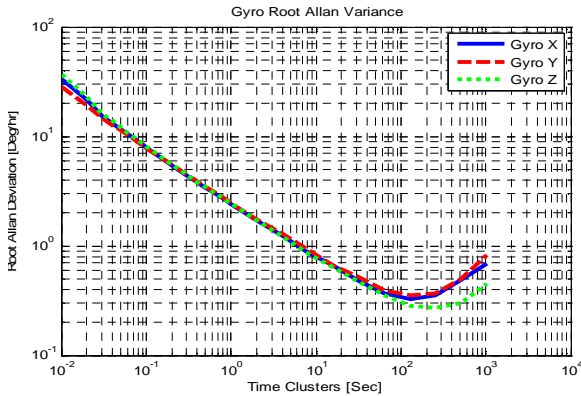


Figure 12: HG1900 gyro and Allan variance analysis

Table 7: Allan variance and identified noise square-root variance for HG1900 gyro axes

Gyro		X	Y	Z	Average
N	[$^{\circ}/\sqrt{\text{hr}}$]	0.045	0.054	0.04	0.05
B	variance [$^{\circ}/\text{hr}$]	0.514	0.551	0.421	0.495
	time constant [s]	192	192	192	192
K	[$^{\circ}/\text{hr}/\sqrt{\text{hr}}$]	2.18	3.126	1.846	2.384

The HG1900 gyro measurements are dominated by angle random walk noise for up to 190 sec. Bias instability of the gyros starts after $\tau=192$ sec. Therefore, it is expected that after a 3 minute static period, the attitude angles, especially yaw, will start to wander. When the time cluster reaches $\tau=210$ sec, the Allan variance of three axes diverge, while the z-axis gyro (green dot curve) has a rate random walk almost twice that of the other two gyros. As shown in Table 7, the angle random walk is $0.05^{\circ}/\sqrt{\text{hr}}$, which shows an uncertainty similar to the HG1700 IMU. The HG1700 gyros thus have long-term stability substantially better than that of the HG1900 gyros. However, the HG1900 gyro measurements are biased by two additional long-term errors, B and K; hence, its error modeling is more complex than for the HG1700.

4.2.3. MicroStrain 3DM-GX2 MEMS IMU

The MicroStrain 3DM-GX2 is a low-cost 6-DOF MEMS IMU with medium to high performance. The 3DM-GX2 also has three orthogonal magnetometers, and six independent A/D converters (one for each sensor). Error

budget analysis for MEMS IMUs usually focuses on the gyros, because the accelerometers performance is not significantly different. According to the product specifications in Table 3, this sensor has a gyro bias instability of $0.2\%/ \text{sec}$ and angle random walk of $3.5^{\circ}/\sqrt{\text{hr}}$. The accelerometer has bias instability of 0.01 g ; almost ten times worse than tactical grade IMUs. For five hours of static accelerometer data, the Allan variance results are shown in Figure 13. The characteristics of the accelerometers are summarized in Table 8.

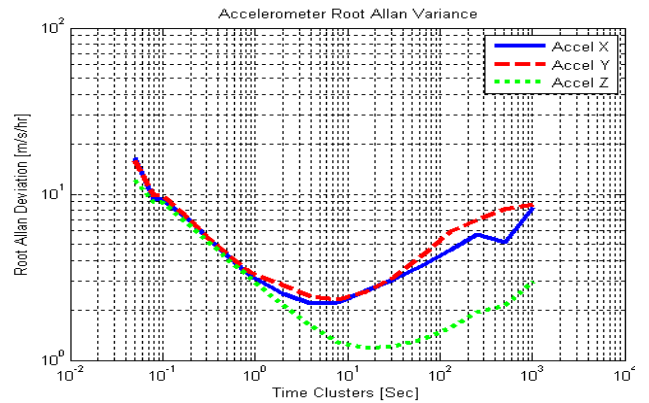


Figure 13: MicroStrain 3DM-GX2 accelerometer and Allan variance analysis

Figure 13 shows that the accelerometer outputs are almost immediately corrupted by quantization noise, turn-on bias, and for roughly the next 8 sec, they all experience a velocity random walk. Following this, all axes experience a flicker noise in the time domain of up to 10 sec.

Table 8: Allan variance and identified noise square-root variance for MicroStrain 3DM-GX2 accelerometer axes

Accelerometer	X	Y	Z	Average	
Q	[m/hr]	0.02	0.26	1.52	0.60
N	[m/s/ $\sqrt{\text{hr}}$]	0.08	0.07	0.07	0.07
B	variance[m/s/hr]	3.42	3.62	1.80	2.94
	time constant [s]	4.5	9	18	10.5
K	[m/s/hr/ $\sqrt{\text{hr}}$]	13.56	29.70	5.70	16.32

In times of less than 200 sec, the output noise is acceleration random walk of average $K=16.3\text{ m/s/hr}/\sqrt{\text{hr}}$. The z-axis accelerometer exhibits an acceleration random walk almost triple that of the other two accelerometers. This is likely caused by gravity that constantly and randomly drifts the Z-axis.

A log-log plot of the three axes gyros of the 3DM-GX2 Allan standard deviation versus cluster time is shown in Figure 14. Based on the plot, the random characteristics of the gyro are showed in Table 9. Figure 14 shows that similar to the accelerometers, the gyro outputs are corrupted by turn-on quantization bias. For roughly the next 40 sec, they all experience an angle random walk.

When the time cluster reaches $\tau=40$ sec, the Allan variance deviations of the three axes diverge. Afterwards, the gyros exhibit a short term instability, which tends to dominate the output noise after about 50 sec in x-axis, 72 sec in y-axis, and 144 sec in z-axis.

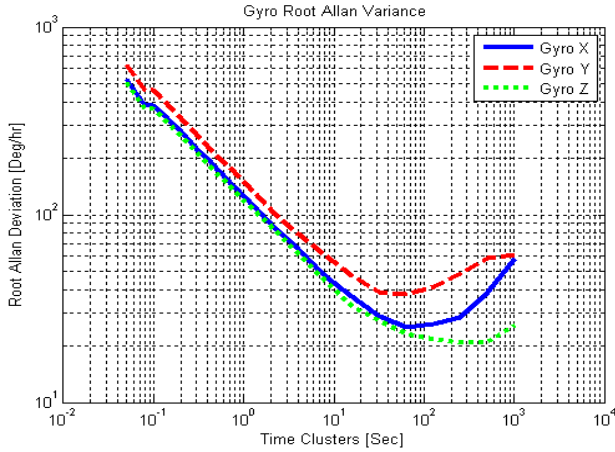


Figure 14: MicroStrain 3DM-GX2 gyro and Allan variance analysis

This bias instability describes the sensitivity of the gyro bias changing along different axes over a specified period of time. A bias instability of an average 43 %/hr means that the bias in the next hour is a random variable with expected value B and the standard deviation of σ_B . Over the long term, this noise appears as a first-order Gauss-Markov process in the gyro bias, with time constant of 90 sec. The initial upward slope of approximately $+1/2$ indicates that the output noise in long term is predominately driven by a rate random walk of average 145 %/hr/ $\sqrt{\text{hr}}$. Our study of this MEMS IMU confirmed that angle random walk error and bias instability are the most important sources of error over short-times; while the angle random walk error is the lower bound of uncertainty.

Table 9: Allan variance and identified noise square-root variance for MicroStrain 3DM-GX2 gyro axes

Gyro	X	Y	Z	Average	
Q [°]	0.18	0.23	0.18	0.19	
N [°/ $\sqrt{\text{hr}}$]	3.54	4.23	3.17	3.64	
B	variance [°/hr]	39.96	58.16	32.73	43.49
	time constant [s]	55	72	144	90
K [°/hr/ $\sqrt{\text{hr}}$]	198.63	99.92	136.03	144.86	

5. PERFORMANCE ANALYSIS

Once the Allan variance analyses of all IMUs were complete, the stochastic models for different components of the IMUs were applied in the loosely-coupled EKF of the Geo-LDV system to generate TSPI data. The amplitude of random walk coefficients were directly used

in the system noise covariance matrix with respect to the corresponding sensor. We expected that the coupled GPS/IMU can obtain TSPI accuracies of 20 cm and 0.2 °. Considering Eq. (12), the EKF used in the Geo-LDV is based on a flexible state complementary filter, including: 12-dimensional navigation TSPI error; 3-dimensional anomalous gravity; 3-dimensional accelerometer residual scale factor; 15-dimensional accelerometer moving bias; 3-dimensional gyro residual scale factor; and 15-dimensional gyro moving bias.

To assess the Allan variance based IMU error characteristics, several datasets were collected with all IMU's. The goals of the experiment were performance analysis of IMUs, comparison analysis of IMUs, and stability analysis of the Geo-LDV in free inertial mode. We utilized three configurations of the Geo-LDV product. The first consisted of a dual-frequency GPS measurement engine coupled with both the HG1700 and HG1900 IMU's. The third consisted of a single-frequency GPS measurement engine coupled with the MicroStrain 3DM-GX2. We were able to run the Microstrain configuration with either the HG1700 or the HG1900 configuration simultaneously in any given run. Thus we compare the HG1700 with the Microstrain and the HG1900 with the Microstrain.,

5.1. HG1700 AND MICROSTRAIN IMUs

Figure 15 shows the 2-Dimensional RMS positioning error between HG1700 and MicroStrain IMUs for the 12.5 km trajectory. Notice that the MicroStrain IMU was coupled with L1 GPS data.

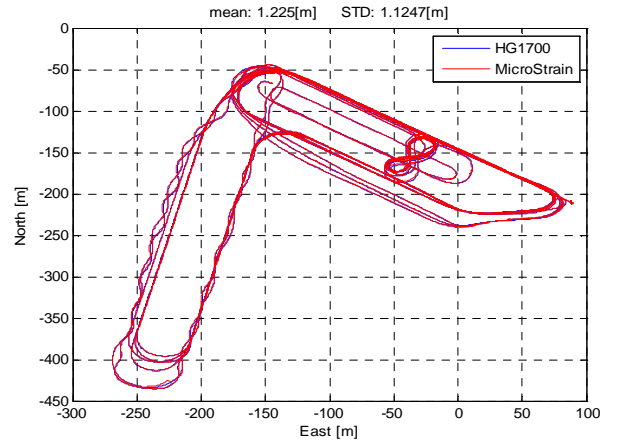


Figure 15: Trajectory comparison: 2-Dimensional RMS positioning error between HG1700 and MicroStrain

Table 10 presents the statistical analysis of the TSPI solution of two IMUs after the initial tuning period of 300 sec. The average RMS of fit in the position, velocity and attitude of about 1.2 m, 0.2 m/s and 1.2 °, respectively, are computed for the selected period.

Table 10: Statistical analysis of the navigation parameters between HG1700 and MicroStrain IMUs

Navigation parameter	Component	RMS Mean \pm STD
Position [m]	East	-0.08 \pm 0.35
	North	0.14 \pm 0.50
	Down	-0.65 \pm 1.39
Velocity [m/s]	Ve	0.02 \pm 0.17
	Vn	-0.01 \pm 0.22
	Vd	-0.01 \pm 0.06
Attitude [deg]	Roll	-0.95 \pm 0.35
	Pitch	0.50 \pm 0.19
	Yaw	-1.03 \pm 1.55

5.2. HG1900 AND MICROSTRAIN IMU's

Table 11 presents the statistical analysis of the TSPI solution of two IMUs for 10.5 km trajectory after initial tuning. The average RMS of fit in the position, velocity and attitude of about 0.58 m, 0.31 m/s and 1.8 °, respectively, are computed for the selected period. Based on the results presented in Table 11, it can be concluded that the MicroStrain MEMS IMU can provide steady navigation accuracy mostly in low maneuver conditions, but in high dynamic situation the results are less accurate.

5.3. NAVIGATION PERFORMANCE DURING GPS OUTAGES

To assess the calibration quality of IMUs using Allan variance, simulated GPS data gaps of 1, 2, 5, and 10 minutes were introduced to each configuration. To examine the real performance, the GPS gap was induced after the filter was tuned and during dynamic maneuvers. Table 12 summarizes the maximum drift observed for TSPI solutions at the end of the corresponding GPS gap period.

Table 11: Statistical analysis of the navigation parameters between HG1900 and MicroStrain IMUs

Navigation parameter	Component	RMS Mean \pm STD
Position [m]	East	0.01 \pm 0.39
	North	-0.01 \pm 0.36
	Down	-0.12 \pm 0.65
Velocity [m/s]	Ve	-0.01 \pm 0.25
	Vn	-0.001 \pm 0.36
	Vd	0.002 \pm 0.23
Attitude [deg]	Roll	1.69 \pm 0.38
	Pitch	1.30 \pm 0.34
	Yaw	1.32 \pm 1.13

The results show that the HG1700 IMU drifts less than 0.1 ° in pitch/roll, and 0.2 ° in heading after 10-minutes of GPS outage. This is due to high bias instability of its gyros that keeps the attitude errors small. These results were in the range of the manufactures' specification (http://www.meridware.com.tw/Documents/Papers/HG1700_SPAN58.pdf). A comparison between HG1700 and HG1900 shows that the HG1900 in free-inertial mode drifts at a larger rate in all navigation components than the HG1700, due to its MEMS grade gyros. For the MicroStrain IMU, considering the gyro bias instability of 43.5 °/hr and rate random walk of 144.859 °/hr/ $\sqrt{\text{hr}}$, (see Table 9), we expected the attitude to drift about 12 ° after 10-minutes. The overall consistency of the TSPI solution provided in Table 12 at the end of 1, 2, 5 and 10-minutes GPS outages shows that the Allan variance analysis resulted in a reliable estimation of HG1700, HG1900 and MicroStrain MEMS sensors error characteristics.

6. CONCLUSION

The Geo-LDV is a GPS/IMU navigation system based on a loosely coupled EKF, designed to provide accurate TSPI solution, e.g., 20 cm in position and 0.2 ° in attitude.

Table 12: The maximum drift of TSPI solutions after GPS outages

Geo-LDV performance during GPS outages		Position [m]			Velocity [m/s]			Attitude [deg]		
		East	North	Down	Ve	Vn	Vd	Roll	Pitch	Yaw
HG1700 (AG58)	1-minute	5.2	2.73	1.45	0.11	0.07	0.08	0.01	0.02	0.04
	2-minutes	9.36	38.08	3.14	0.10	0.10	0.12	0.01	0.02	0.06
	5-minutes	30.78	89.08	11.32	0.10	0.41	0.65	0.03	0.02	0.1
	10-minutes	209.03	156.5	44.32	1.05	0.23	0.72	0.06	0.04	0.17
HG1900 (CA29)	1-minute	6.6	3.90	3.74	0.42	0.28	0.41	0.02	0.01	0.35
	2-minutes	5.17	53.54	12.89	0.47	0.66	0.63	0.03	0.04	0.6
	5-minutes	32.74	41.88	74.9	0.40	0.32	0.88	0.03	0.04	1.0
	10-minutes	1618.3	356.4	120.0	6.04	4.8	4.41	0.21	0.22	12.1
MicroStrain (3DM-GX2)	1-minute	10.25	77.9	1.56	1.27	1.19	1.88	0.56	0.49	3.56
	2-minutes	26.21	2271.1	1.65	1.53	1.64	2.34	0.74	0.87	5.23
	5-minutes	1106	1566	17.6	20.64	1.93	17.27	1.81	1.95	9.37
	10-minutes	2000	15000	250	44.1	33.12	81.3	2.75	2.69	60

Three grades of IMU were considered for the system: a tactical grade HG1700, a MEMS HG1900, and a low-cost consumer-grade MicroStrain 3DM-GX2 MEMS IMU. To reach to the desired accuracy, this paper explored the development of an advanced IMU error-budget analysis and calibration toolbox for performance validation of in-the-field operations.

To estimate deterministic errors, we took advantage of the known magnitude of the measured acceleration and angular velocity for an IMU at rest. In order to avoid the ill-conditioning problem, a Total Least Squares (TLS) approach was developed. The random error sources of the IMUs were identified through Allan variance analysis. To verify our error modeling accuracy, several tests were conducted during GPS reception and GPS outages. Experimental results indicate that for short GPS outages, e.g., less than 1 minute, both the HG1700 and HG1900 can hold the attitude to within the required range, while for longer GPS outages, up to 10-minutes, only the HG1700 can hold the attitude accuracy. These results confirm that IMUs were properly calibrated using coefficients derived by the Allan variance technique. However, both IMUs drift in position over several meters during short GPS outages.

REFERENCES

1. Bock, Y., Macdonald, T., Merts, J., Bock, L., Fayman, J., (2004). Epoch-by-Epoch® Real-Time GPS Positioning in High Dynamics and at Extended Ranges. *The ITEA Journal*, 25(3), pp. 37-45.
2. Dorobantu, R.; Gerlach, C., (2004). Characterization and Evaluation of a Navigation-Grade RLG SIMU; *European Journal of Navigation*, 2(1), pp. 63-78.
3. Fayman, J.A., Bock, L., Westin, C.S., Ratcliff, W.B., (2007). Epoch-by-Epoch® Network-Centric Positioning Unit for FCS Testing. *ITEA Symposium*, Lihue, Kauai, HI.
4. Flenniken IV W.S., Wall J.H., Bevly D.M., (2005). Characterization of Various IMU Error Sources and the Effect on Navigation Performance. *Proc. of ION GNSS*, CD-ROM.
5. Grewal, M. and A. Andrews, (2010). How Good Is Your Gyro [Ask the Experts]. *Control Systems Magazine*, IEEE, 30(1).
6. Hou, H., (2004), Modeling Inertial Sensors Errors Using Allan Variance, M.Sc. thesis, Department of Geomatics Engineering, University of Calgary, Canada, UCGE Report 20201.
7. IEEE Standard Definitions of Physical Quantities for Fundamental Frequency and Time Metrology. *IEEE Std 1139™-1988*.
8. Jekeli, C., (2001). *Inertial Navigation Systems with Geodetic Applications*, Walter de Gruyter: Germany.
9. Kim, H, J. G. Lee, C. G., Park (2004). Performance Improvement of GPS/INS Integrated System Using Allan variance Analysis. *International Symposium on PS/GNSS*, Sydney, Australia.
10. Mathur N.G, (1999). Feasibility of Using a Low-Cost Inertial Measurement Unit with Centimeter Accuracy Differential Global Positioning System. PhD Dissertation, Ohio University, Athens, Ohio.
11. Naranjo, C.C.M, (2008). Analysis and Modeling of MEMS based Inertial Sensors, Stockholm, Signal Processing, KTH. School of Electrical Engineering.
12. Schaffrin B., (2006). A Note on Constrained Total Least-Squares Estimation. *Linear Algebra and its Applications*. Volume 417, Issue 1(1), pp. 245-258.
13. Shin E.H., (2001). Accuracy Improvement of Low Cost INS/GPS for Land Applications. UCGE Report No. 20156, Dept. of Geomatics Engineering, University of Calgary, Canada.
14. Skog I. and P. Händel, (2006). Calibration of a MEMS Inertial Measurement Unit. *IMEKO XVIII World Congress*, Rio de Janeiro, Brazil, pp. 17–22.
15. Syed Z. F., Aggarwal P., Goodall C., Niu, X., and El-Sheimy, N., (2007). A New Multi-Position Calibration Method for MEMS Inertial Navigation Systems. *IOP PUBLISHING, Meas. Sci. Technol.* 18 (2007), pp. 1897–1907.
16. Woodman, O. J, (2007). An introduction to inertial navigation. Technical Report UCAM-CLTR-696, University of Cambridge, Computer Laboratory.
17. Yi, Y., (2007). On Improving the Accuracy and Reliability of GPS/INS-based Direct Sensor Georeferencing. Ph.D. Dissertation, The Ohio State University, Columbus, OH.
18. Zhang, X., Li, Y., Mumford, P., & Rizos, C., (2008). Allan Variance Analysis of Error Characteristics of MEMS Inertial Sensors for an FPGA-based GPS/INS System. *Int. Symp. on GPS/GNSS*, Yokohama, Japan, pp. 127-133.
19. Zhang, H., Wu, Y., Wu, M., Wu, W., Hu X., (2010). Improved Multi-position Calibration for Inertial Measurement Units. *IOP PUBLISHING, Meas. Sci. Technol.* 21 (2010), pp.15107-15118.